Engineering Optical Absorption in Late Transition-Metal Nanoparticles by Alloying

Citation for the original published paper (version of record):
Tiburski, C., Langhammer, C. (2023). Engineering Optical Absorption in Late Transition-Metal Nanoparticles by Alloying. ACS Photonics, 10(1): 253-264.
http://dx.doi.org/10.1021/acsphotonics.2c01597

ACS Photonics

pubs.acs.org/journal/apchd5

Article

Engineering Optical Absorption in Late Transition-Metal Nanoparticles by Alloying

Christopher Tiburski and Christoph Langhammer*

Cite This: https://doi.org/10.1021/acsphotonics.2c01597

Read Online

ACCESS | Metrics & More | Article Recommendations | Supporting Information

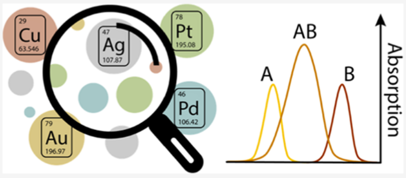

ABSTRACT: Alloying is an increasingly important handle to engineer the optical properties of metal nanoparticles that find applications in, for example, optical metamaterials, nanosensors, and plasmon-enhanced catalysis. One advantage of alloying over traditionally used particle size and shape engineering is that it, in principle, enables tuning of optical properties without a spectral shift of the localized surface plasmon resonance, which is important for applications where a specific spectral band is targeted. A second advantage is that alloying simultaneously enables adjustment of nanoparticle electronic, chemical, mechanical, and light absorption properties. However, a systematic survey of the impact of alloying on light absorption in metal nanoparticles does not exist, despite its key role in applications that include photothermal therapy, plasmonic heat generation, and plasmon catalysis. Therefore, we present here the systematic screening of the light absorption properties of binary late transition-metal alloys composed of Au, Ag, Cu, Pd, and Pt in the visible spectral range, based on a combination of experiments and finite-difference time-domain simulations, and discuss in detail the underlying physics. By studying these 10 alloy systems for 14 different nanoparticle sizes, we find that most nanoparticles experience a maximal absorption efficiency at around 80 nm particle diameter, and that most alloy systems outperform their neat constituents, with integrated absorption enhancement factors of up to 200%. This highlights the untapped potential of alloying for the engineering of light absorption in nanoparticles, and the presented material screening constitutes a resource for the rational selection of alloy systems with tailored absorption properties.

KEYWORDS: *nanoparticles, plasmonics, nanoalloys, absorption efficiency, optical response, finite-difference time-domain simulation*

■ INTRODUCTION

Metal nanoparticles with their ability to both sustain localized surface plasmon resonances (LSPR) and steer catalytic surface reactions are today used in a wide range of applications across many fields of science and technology. Focusing here on harvesting the specific traits of the LSPR, such as its ability to enhance optical near-fields and generate hot electrons, as well as to photothermally generate heat, we find metal nanoparticles in applications like photovoltaic devices,[1−3] optical metamaterials,[4] optical sensing,[5,6] nanomedicine,[7] and plasmon-enhanced catalysis.[8−10] Many of these applications rely on the significantly increased optical absorption cross-sections at visible frequencies induced by LSPR, which enhance energy absorption that in turn leads to, for example, heat generation at the nanoscale that can be harvested in photothermal catalysis or nanomedicine.[11−14] Hence, it is of technological relevance to find ways to maximize or optimize the optical absorption cross-sections of metal nanoparticles. The most common and well-established way to do this is to engineer the shape or size of plasmonic metal nanoparticles since these parameters control the ratio between absorptive and scattering LSPR decay.[15−17] It has also been shown that the selection of metallic element has a significant impact on the absorption versus scattering properties via the abundance of inter- and intra-band transitions in the spectral range of interest.[18−20]

More recently, another handle for steering the optical/plasmonic properties of metal nanoparticles has started to receive more attention—alloying.[21−23] This concept, which is known since the Bronze age, is the process of mixing two or several elements at the atomic level to obtain material properties and functions that cannot be obtained by a single element alone. Therefore, it has been widely used to optimize, for instance, the strength and ductility of metals,[24] as well as their high-temperature compatibility in applications like gas turbines.[25] At the nanoscale, alloying is widely used in heterogeneous catalysis to engineer activity and selectivity of surface reactions,[26] in hydrogen sensors,[27] in electrochemical desalination,[28] and in biological applications like bioimaging or photothermal therapy.[29] Here, the increasing availability of colloidal synthesis routes of alloy nanoparticles[30−32] is an important driver of this development. Returning to the application of the alloying concept in nano-optics and plasmonics, we have recently reported a systematic first-principles calculations based study of the complex dielectric

Received: October 11, 2022

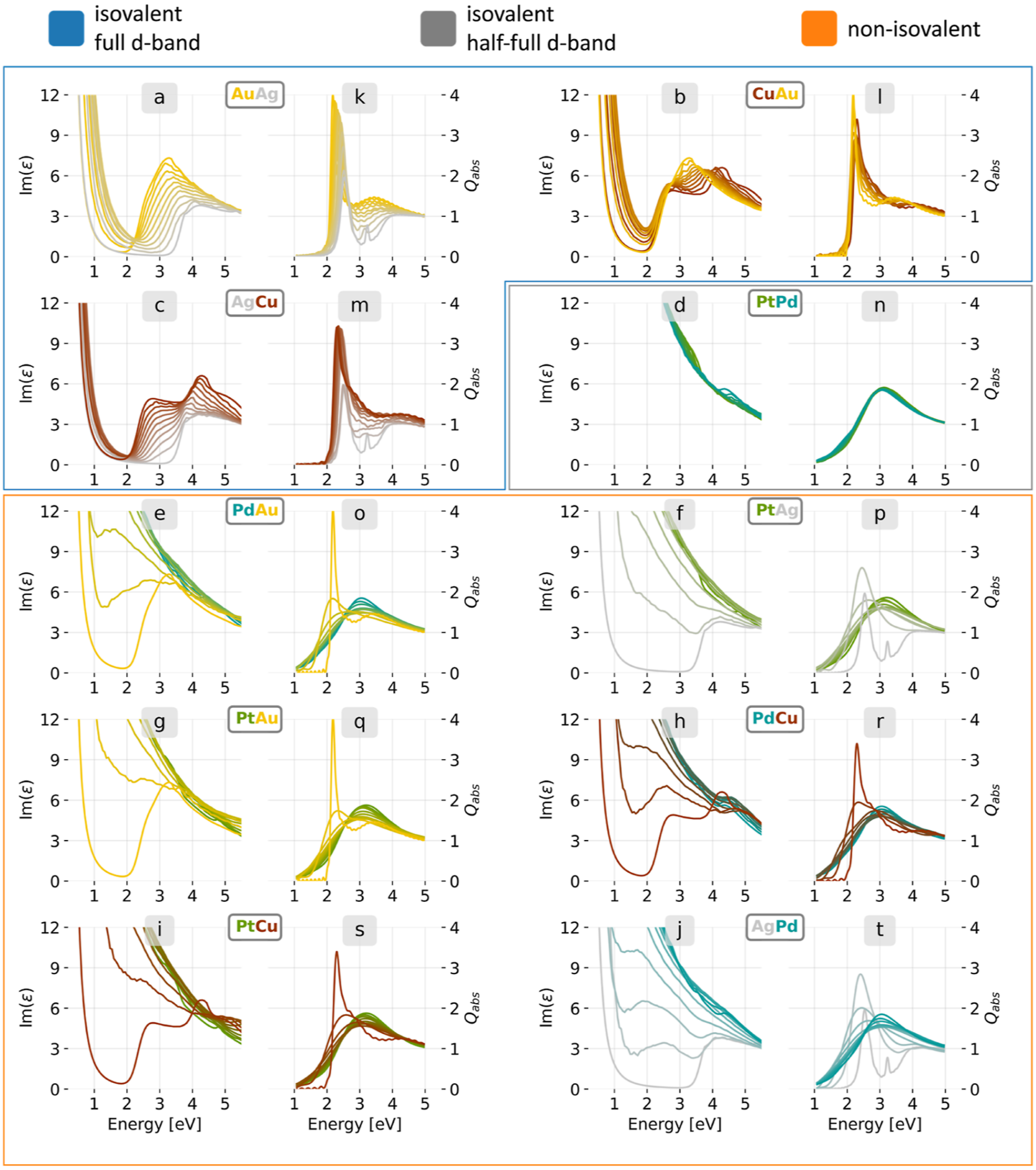

Figure 1. Imaginary part of the complex dielectric functions of the 10 considered alloy systems plotted in 10 at. % concentration steps (a−j) together with their respective absorption efficiency, Q_{abs}, spectrum calculated for a disk with a diameter of 80 nm and a height of 25 nm on a SiO_2 substrate using FDTD (k−t). The key difference between the isovalent full d-band (a−c,k−m), isovalent half-full d-band (d,n), and non-isovalent (e−j,o−t) systems is that the isovalent systems show only changes in the fine structure of the imaginary part of the dielectric function, and their overall shape is retained upon alloying, which translates into absorption spectra whose overall shape is maintained across the whole alloy composition range (k−n). In contrast, the non-isovalent systems exhibit significant changes in the overall shape of the imaginary part of the dielectric function (e−j), which translate into systematically changing absorption spectra (o−t). The dielectric functions can be downloaded on https://sharc.materialsmodeling.org/alloy_dielectric_functions.

functions of late transition-metal alloys,[33] and Jian et al. reported a first-principles study of non-radiative LSPR decay in the AgCu alloy system.[34] However, beyond these studies that highlight the potential of alloying to engineer non-radiative LSPR decay and thereby the optical absorption properties of metal nanoparticles, a systematic study of the impact of alloying on light absorption in nanoplasmonic systems is lacking in the literature. Therefore, in this work, we systematically screen the non-radiative LSPR decay in 10 binary late transition-metal alloy nanoparticle systems as a function of alloy composition, as well as spectral position of the LSPR. For this purpose, as a first step, we nanofabricated quasi-random arrays of three selected alloy nanoparticle systems in 10 at. % composition intervals and compared their experimentally determined optical absorption efficiencies to the corresponding values obtained by finite-difference time-domain (FDTD) simulations to validate the entire approach, using the complex dielectric functions from Rahm et al.[33] as the input. For this validation, we selected the three alloy systems AuAg, PdPt, and AuPd since they represent isovalent full-d-band, isovalent half-full-d-band, and non-isovalent systems, respectively. Based on the found good agreement between experiment and theory, we then extended our FDTD simulations by the seven additional alloy systems AuCu, AgCu,

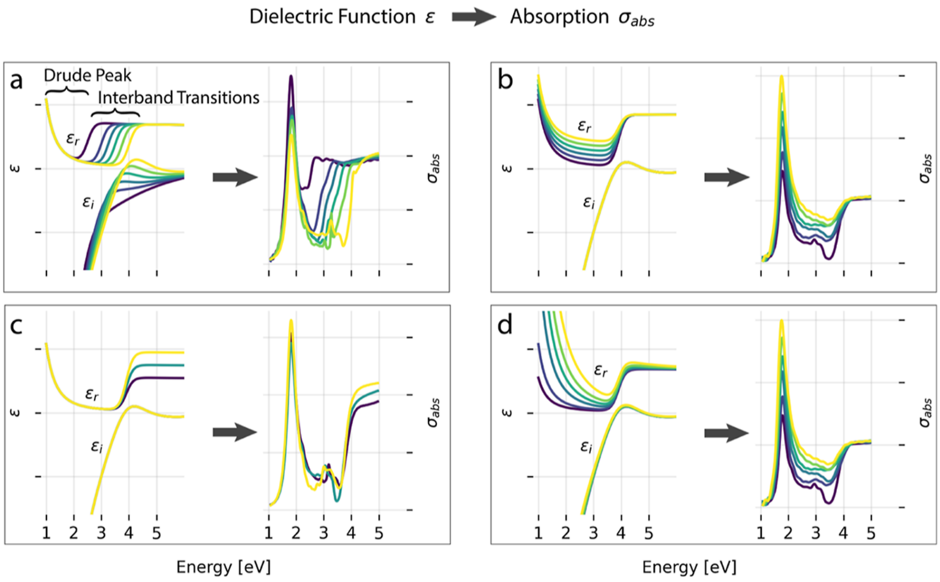

Figure 2. Arbitrary dielectric functions modeled as a systematically changed combination of intra- and interband transitions to induce systematically changing features, using a correspondingly modeled Ag dielectric function as the starting point.[38] The functions are plotted together with the correspondingly simulated absorption spectra for a disk with a diameter of 140 nm and a height of 25 nm on a SiO_2 substrate using FDTD.[38] A shift of the interband transition threshold energy (a) leads to a corresponding shift of the energy at which the absorption rises due to interband transitions. Increasing the intensity of the Drude peak by either changing its width (d) or its height (b) impacts mainly LSPR absorption peak intensity. Increasing the imaginary part of the dielectric function above the interband transition energy mainly increases the absorption above this energy threshold (c).

PtAg, PtAu, PdCu, PtCu, and AgPd and screened systematically the dependence of the optical absorption efficiency on the alloy composition in 10 at. % steps for, in the end, 14 different particle sizes to thereby cover a wide LSPR spectral range.

RESULTS AND DISCUSSION

The pure late transition metals of interest in this study, that is, Au, Ag, Cu, Pt, and Pd, can be classified into two categories: (i) Pd and Pt with strong interband transitions across the entire spectral range of interest due to their d-band only being partially filled and therefore crossing the Fermi level and (ii) Ag, Au, and Cu with weak interband transitions in the visible energy range due to their completely filled d-band below the Fermi level.[18,19] This fundamental difference in the band structure is reflected in the complex dielectric function as a wide Drude peak for Pt and Pd and a narrow Drude peak for Au, Ag, and Cu, with a region of low absorption and damping before the onset of interband transitions at 2.4,[35] 3.98,[36] and 2.15 eV,[37] respectively, that increases the imaginary part of the dielectric function beyond this threshold (Figure 1a–j, data for dielectric functions from Rahm et al.[33]). As a consequence, we can divide the 10 binary alloy systems of these five metals into isovalent and non-isovalent systems, where the isovalent alloys can be further categorized into isovalent with full d-band constituents [AuAg, AgCu, and AuCu (Figure 1a–c)] and isovalent with half-full d-band constituents [PdPt (Figure 1d)]. As the main observation, we see that the imaginary part of the dielectric function of the isovalent systems shows only small (Figure 1a–c) to minor (Figure 1d) changes as a function of alloying, and the overall shape is maintained, whereas for the non-isovalent systems, more dramatic changes occur (Figure 1e–j, more details in a study by Rahm et al.[33]).

To investigate how the evolution of the alloy-specific dielectric functions impacts the light absorption properties of corresponding alloy nanoparticles, in a first step, we calculated absorption efficiency spectra for a 25 nm high cylindric nanoparticle—a "nanodisk"—with a diameter of 140 nm on the SiO_2 substrate for the 10 binary alloys of interest, in 10 at. % composition intervals, using the dielectric functions calculated by Rahm et al. as the input. We then plot the obtained spectra in terms of the absorption efficiency (rather than absorption cross-section), which is the cross-section divided by the projected particle area (Figure 1k–t). This value is more useful since it directly reveals which particle size that is most efficient in absorbing light, whereas the absorption cross-section just increases with the particle size (Figure S1). Furthermore, working with the absorption efficiency is an effective way to directly compare calculated absorption values with experimentally obtained ones, as we do further below, since nanoparticle surface coverage effects, and so forth, can be divided out.

Analyzing the obtained series of spectra for all 10 binary alloys reveals that for the isovalent systems, the overall shape of the spectra is similar across the whole compositional range (Figure 1k–n). The difference between full and half-full d-band can be seen as the full d-band systems AuAg, AgCu, and AuCu (Figure 1k–m) showing a strong peak in their absorption, whereas the half-full d-band system PdPt (Figure 1n) exhibits a wide peak with lower intensity. In contrast, the non-isovalent systems exhibit distinct changes in the overall shape of their absorption spectra, as well as in terms of absolute absorption efficiencies (Figure 1o–t). As a general observation, we note that the strong and spectrally narrow absorption peak in the pure Au, Cu, and Ag systems strongly decreases in intensity and instead spectrally broadens significantly with increasing Pd or Pt content. This effect can be attributed to the abundant interband transitions in Pt and Pd across the visible range, reflected as a lack of distinct onset of interband transitions in the dielectric function with increasing Pd or Pt content in the alloys above 20 at. %.

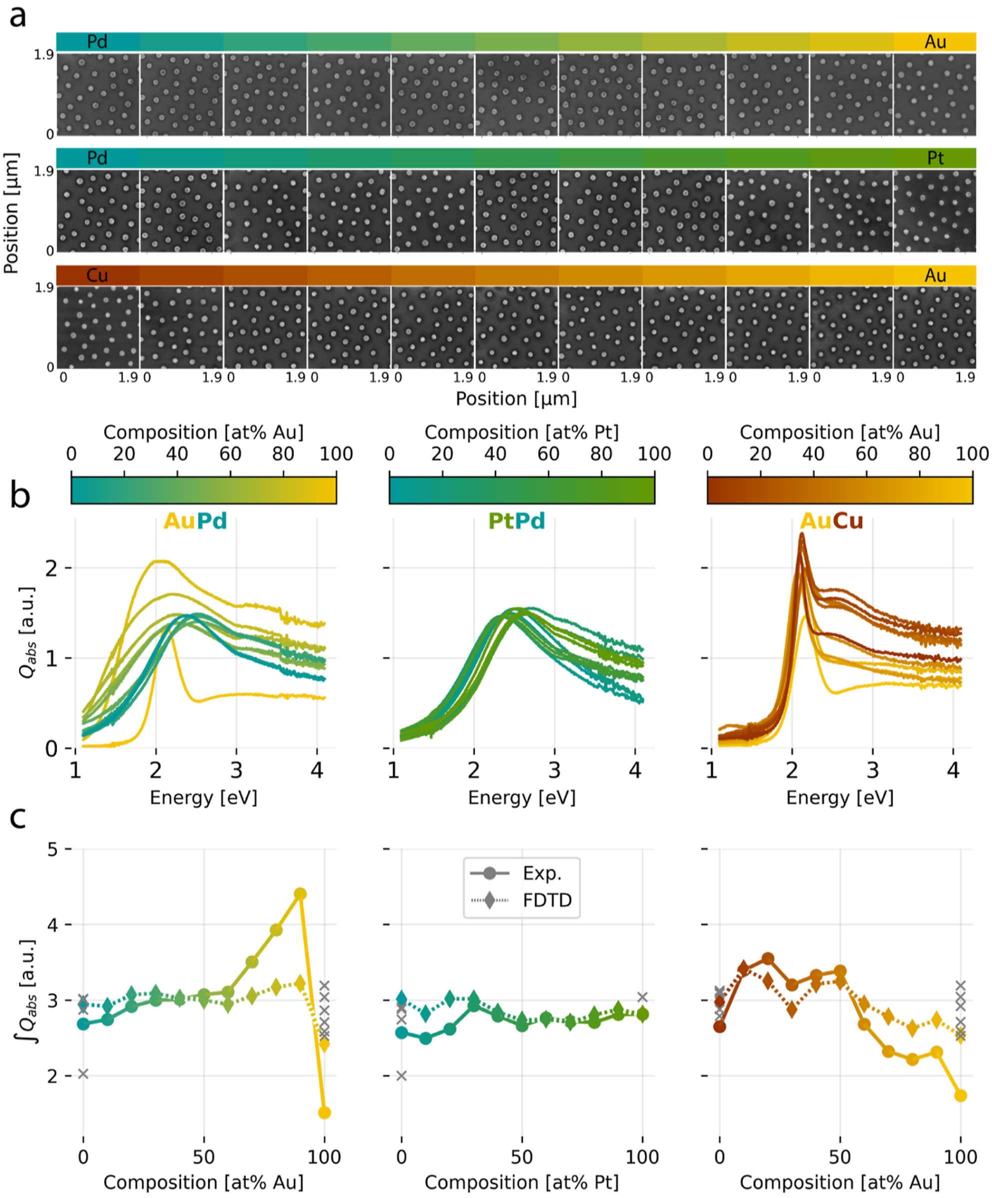

Figure 3. (a) SEM images of the three alloy systems AuPd, PdPt, and AuCu taken in 10 at. % composition steps used to determine the average disk diameter for each alloy system after annealing and to verify the pristine condition of the particles. The obtained diameters were subsequently used as the input for the corresponding FDTD simulations. (b) Absorption efficiency spectra measured for the samples shown in (a). They reveal the evolution of alloy optical response in 10 at. % composition steps. (c) Experimentally obtained absorption efficiency integrated over the photon energy range 1.1−4.1 eV for all three alloy systems, compared to the corresponding values obtained from FDTD simulations that used the mean disk diameter obtained from SEM images depicted in (a) together with the dielectric functions from a study by Rahm et al.[33] as the input. Also shown (gray × markers) are calculated integrated absorption efficiency values obtained from FDTD simulations of the pure metals, using dielectric functions from the literature for Au,[41−46] Pd,[42,43,47,48] Pt,[43,48] and Cu[41−43,46,49] as the input. The peak intensities in the experimental data are scaled to the peak intensity maxima of the FDTD data (for unscaled raw data, see Figures S3 and S4).

This is the consequence of a strong shift of the d-band center closer to the Fermi level, resulting in a lower energy needed for the interband transition when a full d-band metal is alloyed with Pd.[33]

To understand the observed changes and trends in the calculated absorption efficiency spectra as a function of alloy composition and relate them back to corresponding changes in the dielectric function, we calculated the absorption efficiency spectra based on a range of arbitrary dielectric functions, modeled as a combination of intra- and interband transitions in which we systematically changed specific features. This approach has been successfully used to model the dielectric functions of Ag and Au.[38] Hence, as starting point for this analysis, we modeled the Ag complex dielectric function (details in Supporting Information Section S1: dielectric function model), based on which we calculated the absorption spectrum of a disk with a diameter of 140 nm and a height of 25 nm on a SiO_2 substrate using FDTD. Subsequently, we systematically shifted the interband transition threshold energy by a couple of eV to lower energies, which revealed that the LSPR peak essentially remains unchanged and that only the absorption above the transition energy increases (Figure 2a). In contrast, changing the Drude peak of the dielectric function by either changing its width or the height impacts mostly the

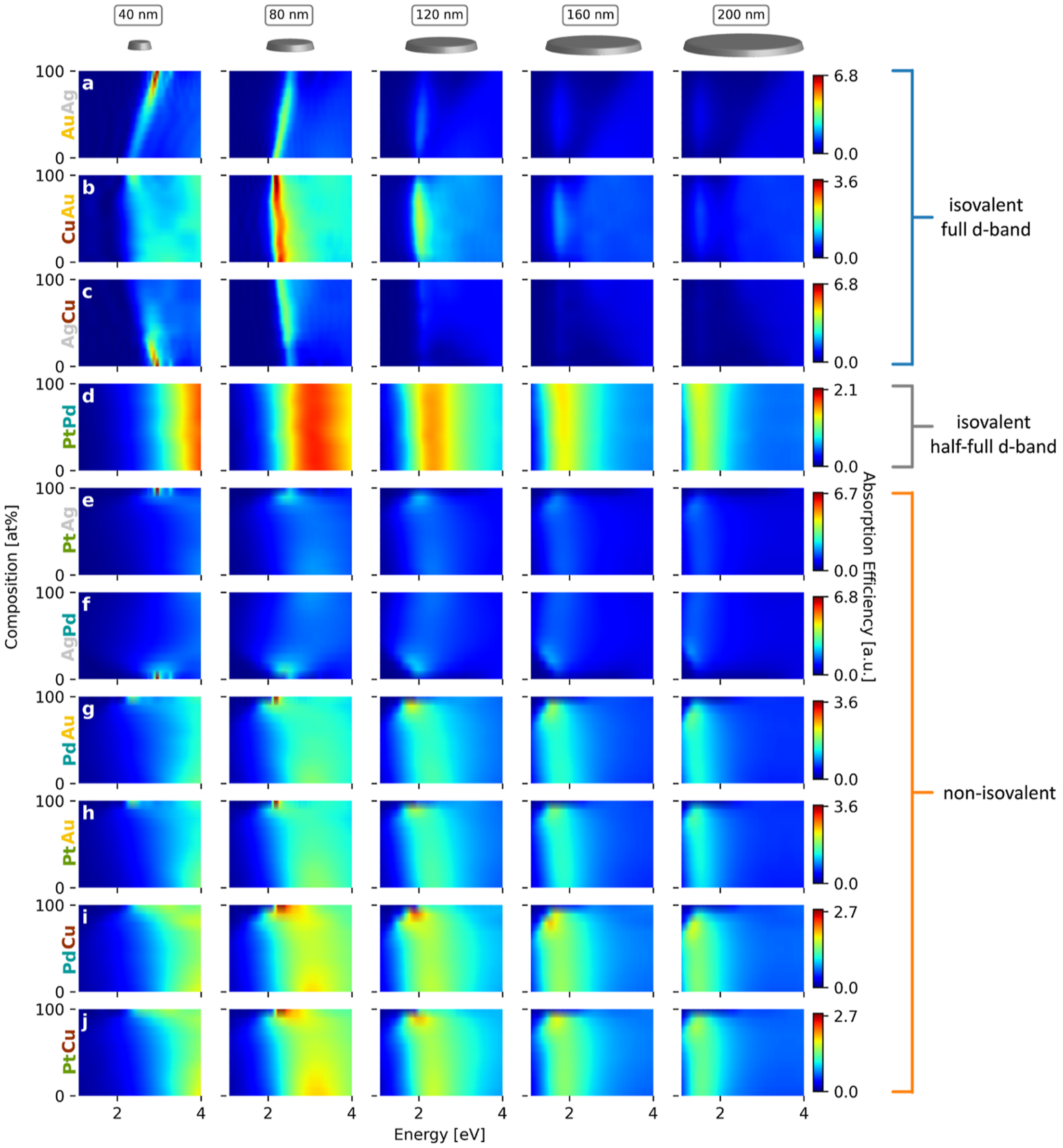

Figure 4. Overview of the absorption efficiency spectra for the 10 binary alloy systems of Ag, Au, Cu, Pd, and Pt calculated by FDTD for a nanodisk with 25 nm thickness on a SiO_2 support and a diameter indicated at the top of the figure, for 10 at. % alloy composition increments (a−c). The isovalent alloys without interband transitions in the visible range, AuAg, CuAu, and AgCu, exhibit a narrow peak with the highest absorption efficiency for disks with 80 nm diameter. All three alloys also show a linear shift of the peak position upon alloying that is most pronounced for 40 and 80 nm diameters. (d) The isovalent system PdPt is characterized by an interband transition continuum across the entire considered energy range for both constituents, which is the reason for the wide absorption peak via increased interband damping of the LSPR. (e−j) Non-isovalent alloys exhibit a strongly non-linear behavior in the absorption peak position as a function of alloy composition due to a corresponding non-linear evolution of their density of states.[33] Furthermore, adding as little as 10 at. % Pd or Pt to Ag, Au, or Cu leads to significant absorption peak broadening and a lowering or increase in the peak intensity for small or large disk diameters, respectively.

LSPR peak intensity (Figure 2b/d). Finally, increasing the imaginary part of the dielectric function above the interband transition energy threshold mainly affects the absolute absorption value in this energy range (Figure 2c).

Projecting these insights now onto the alloy systems, as plotted in Figure 1a−j, reveals that the observed compositional evolution of the alloy dielectric functions is a combination of the effects discussed above and additional more subtle changes in the fine structure of the dielectric functions when going from metal A to metal B. For example, for the case of the isovalent alloy AuAg (Figure 1a,k), the interband transition threshold shifts to higher energies when increasing the Ag content in Au and the Drude peak narrows. This, in turn, leads to decreasing absorption in the energy range around 3 eV. A similar behavior can be seen for the AgCu system and for the same reason (Figure 1c,m). AuCu shows only minor changes in the absorption spectra due to a constant overall shape of the dielectric function across all compositions (Figure 1b,l).

Selecting AuPd (Figure 1e,o) as a representative example for a non-isovalent alloy, we see that even though the dielectric function is changing more drastically, the above simple analysis can largely explain the observed impact on the absorption efficiency. Specifically, the significant broadening of the Drude peak upon increasing the Pd content in Au induces higher absorption in the corresponding energy range. The same effect is apparent for all non-isovalent alloy systems.

Having established this fundamental understanding of the interplay between dielectric function and LSPR absorption, we set out to validate the calculated absorption efficiencies by comparing them to experimental values for (i) AuCu as a representative for an isovalent—full d-band system, (ii) PdPt representing an isovalent—partially full d-band system, and (iii) AuPd representing a non-isovalent system. For this purpose, we fabricated a series of 1 × 1 cm^2 samples using the hole-mask colloidal lithography (HCL) protocol reported and validated for homogeneous alloy nanoparticles earlier.[22,33,39,40] This resulted in quasi-random arrays of alloy disks[22] with a nominal diameter of 140 nm and a height of 25 nm on a SiO_2 substrate (Figure 3a). As a summary of the nanofabrication process that is described in detail in our previous work, where we also have validated the formation of homogeneous alloys,[22] we note that the two metal constituents are evaporated through a mask that defines both position and diameter of the particles, and that the sample subsequently is annealed at 500 °C for 24 h to induce alloy formation (see also the Methods section for details).

To measure the absorption spectra of the nanofabricated series of alloy nanoparticles, we used an integrating sphere mounted onto a spectrophotometer (see the Methods section for details). To both be able to calculate the absorption efficiency for each sample/alloy composition and accurately simulate the corresponding system with FDTD for direct comparison, we acquired scanning electron microscopy (SEM) images of each sample (Figure 3a). This step is of particular importance since the particles slightly change their dimensions during annealing due to recrystallization. As we have reported earlier, the details of this reshaping depend on the specific alloy composition,[33] which means that it leads to a size distribution across the alloy compositions (Figure S2) that has to be explicitly taken into account in the FDTD simulations. As a second aspect, we also use the SEM images to obtain the particle surface coverage information for each specific sample (this is important since slight variations may occur as a consequence of the self-assembly-based mask formation of the HCL nanofabrication method), which we then use to calculate the absorption efficiency spectra (Figure 3b) of each sample according to $Q_{\mathrm{abs}} = \frac{A}{\mathrm{cov}}$, where A is the experimentally measured absorption and *cov* is the particle surface coverage obtained by SEM imaging.

To subsequently compare the experimentally obtained absorption properties of our three alloy systems with the simulated ones, we integrated the efficiency spectra across the 1.1 to 4.1 eV (around 1130 to 300 nm) spectral range and plot the obtained values as a function of alloy composition (Figure 3b). Overall, we find good agreement between experiments and simulations, with the biggest deviation revealing itself in AuPd and AuCu for the more gold heavy alloys. To investigate its origin, we also executed simulations for the pure elements using a range of experimentally determined dielectric functions from the literature for Au,[41−46] Pd,[42,43,47,48] Pt,[43,48] and Cu.[41−43,46,49] Adding the obtained data as individual points to Figure 3c reveals a significant spread, which is the largest for Au and within the range of the observed discrepancy between our experimental and simulated integrated absorption efficiency data. This highlights that the origin of the discrepancy between experiments and simulations in the Au-rich alloys to a large extent is to be found in the limited accuracy of the dielectric function used as the input in the simulations. Furthermore, it also pinpoints the much more far-reaching and important issue of variations in dielectric functions widely used for simulations in nano-optics and plasmonics in general that may yield significantly different results for a single system. Hence, this level of uncertainty is important to always keep in mind to put quantitative comparison with the experimental data into perspective in terms of what kind of agreement that can be expected.[33] The reasons for the significant differences in experimentally determined dielectric functions reported in the literature are to be found in the difficulty to accurately measure a dielectric function since it depends on the sample's fabrication method, sample condition [thickness, roughness, morphology, and state of (surface) oxidation], as well as the used measurement technique.[46,50−54] In addition to these experimental uncertainties, also first principles calculations and FDTD simulations are not completely accurate, altogether explaining our observations.[55]

Since we now have established the general validity of the alloy dielectric functions derived by Rahm et al.[33] for the purpose at hand, we use them to calculate absorption spectra for alloy nanoparticles with the same geometry as above, but for five different particle diameters, that is, 40, 80, 120, 160, and 200 nm, and for all 10 binary alloy systems (Figure 4). This allows us to map the interplay between the alloy composition and particle diameter and thus spectral position of the LSPR.

Starting with the isovalent systems with a fully occupied d-band AuAg, AuCu, and AgCu (Figure 4a−c), we see that the absorption efficiency spectra exhibit a distinct LSPR absorption peak that upon alloying spectrally shifts in a linear fashion, with the slope depending on the particle size. Interestingly, at 80 nm disk diameter, most of the alloys exhibit their strongest peak and thus their highest absolute absorption efficiency. The only exception is alloys with an Ag content above ≈80%, which exhibit the strongest peak already at 40 nm particle diameter. Upon closer inspection, we furthermore notice that a weak absorption peak is visible around 2 eV for the isovalent alloys and also for particle sizes above 120 nm, while it is essentially absent for the pure metals. This is the first indication that alloy systems may exhibit higher absorption than their pure metal constituents.

Turning to the isovalent system PdPt with partially filled d-bands, we find that it also exhibits a clear peak in the absorption efficiency but with significantly lower intensity than AuAg, AuCu, and AgCu (Figure 4d). Furthermore, the peak is much wider and occurs at higher photon energies for 40 and 80 nm particle diameter compared to the isovalent systems with filled d-bands. A simple conceptual explanation for this observation can be found in the model of a metal sphere and the Fröhlich condition,[56] which states that the polarizability and thus the absorption efficiency experience a maximum when

$$Re(\epsilon) = -2\epsilon_{\mathrm{m}}$$

where ϵ_{m} is the dielectric constant of the surrounding medium. Hence, since the real part of the Pd and Pt dielectric function is generally lower (more negative) compared to Au, Ag, and Cu, the Fröhlich condition is met at higher energy (Figure S5). The wider peak is the consequence of the strong interband excitation-induced damping in the metals Pt and Pd.[18]

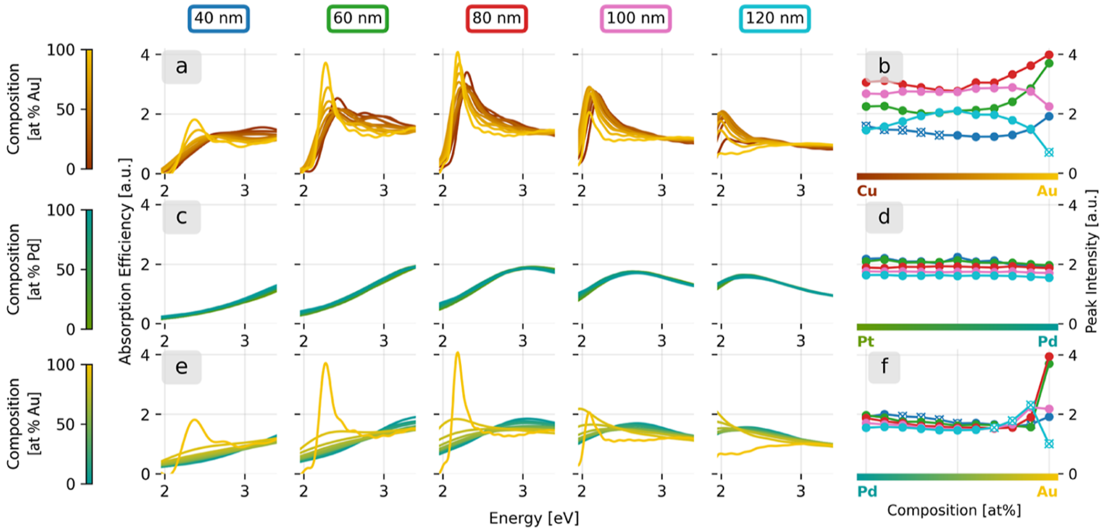

Figure 5. Absorption efficiency spectra for the three systems: (a) AuCu as an isovalent—full d band representative, (c) PdPt as an isovalent—partially full d-band representative, and (e) AuPd as a non-isovalent representative. They are plotted for the whole range of alloy compositions in 10 at. % increments and for five different particle diameters. LSPR peak intensity as a function of alloy composition for (b) AuCu, (d) PdPt, and (f) AuPd. We note that data points marked ⊗ cannot reliably be determined because they are part of a double peak or outside the calculated spectral limit. In the latter case, the values located at the spectral limit are taken as the peak intensity.

Finally, for all non-isovalent alloys (Figure 4e−j), we see distinct broadening of the LSPR peak already at 10 at. % Pt or Pd being added to Ag, Au, or Cu. This broadening is accompanied by a strong decrease in peak intensity. Above 20 at. % Pt or Pd, however, further changes in the alloy absorption efficiency are minimal. Interestingly, in comparison to the isovalent systems, the peak shift in the absorption spectra as a function of composition is also strongly non-linear, in agreement with the observations for corresponding extinction spectra in our earlier work (Figure S6).[33] The reason for this non-linearity is the changes in the density of states for the non-isovalent alloy systems, where already small amounts of Pd in Ag or Au lead to a highly non-linear shift of the d-band edge, which then translates into the peak position and full-width-at-half-maximum of the plasmonic peak.[33] As the last aspect, we note that the relative peak intensity decrease with increasing particle size is less pronounced in these non-isovalent alloys compared to the isovalent alloy systems between Au, Ag, or Cu, as well as compared to neat Au, Ag, or Cu.

To discuss the absorption spectra and how they evolve both as a function of alloy composition and particle size in detail, we again turn to the three representative alloys: (i) AuCu for isovalent—full d band (Figure 5a,b), (ii) PdPt for isovalent—partially full d-band (Figure 5c,d), and (iii) AuPd for non-isovalent systems (Figure 5e,f) and focus on the particle diameter range from 40 to 120 nm since this is the range with the largest changes (cf. Figure 4). We plot the absorption efficiency spectra for all five particle diameters across the whole alloy composition range (Figure 5a,c,e). Analyzing the evolution of the spectra first for AuCu reveals that the highest absorption efficiency is reached for 80 nm particle diameter and that the LSPR absorption peak shifts only slightly when moving from pure Cu to Au (Figure 5a). Interestingly, however, the intensity of the peak develops differently as a function of alloy composition depending on the particle size and thus spectral position of the LSPR (Figure 5b). Specifically, for particles sizes below 100 nm, pure Au shows the highest LSPR absorption peak intensity, which then decreases quickly upon addition of Cu, to then again increase for Cu contents >50 at. %. For particle diameters larger than 100 nm, this trend is inverted, and the pure metals essentially do not exhibit an LSPR absorption peak anymore since in this size regime, radiative LSPR decay dominates completely. Hence, the only notable absorption occurs directly via the interband transitions from the 3d to the 4sp band at higher energies. Interestingly, however, the situation is different for the alloys since they still exhibit a clear LSPR absorption peak even for particle diameters >100 nm. This peak exhibits the highest intensity at alloy compositions around 50 at. % Cu and Au. Notably, we also find a very similar behavior of the AgCu system where the alloys exhibit stronger interband transition-related non-radiative LSPR decay than the pure metals.[34]

The isovalent—partially full d-band PdPt system reveals almost no change in the absorption efficiency spectra upon alloying (Figure 5c). Similarly, particle size only slightly affects peak intensity (Figure 5d). Overall, this behavior is expected and can be explained by the very similar band structure of the two metals Pt and Pd (Figure S7).[57,58]

Turning to the last system, AuPd, we find a very different scenario (Figure 5e). Specifically, alloying Au with just 10 at. % Pd induces a pronounced broadening of the LSPR absorption peak and for as little as 30 at. % Pd in Au the system exhibits an almost identical absorption efficiency spectrum as pure Pd. This is due to the aforementioned non-linear change in the density of states (see Figure 1e,o). The initial dramatic broadening of the absorption peak is also accompanied by a large spectral shift of the peak to higher photon energies, which quickly settles and only slightly changes with further increasing Pd content (Figure S6g). Finally, we notice that the intensity of the LSPR absorption peak stays almost constant across changing alloy compositions and only increases significantly in the step to pure Au, as well as that the absolute peak intensity only very slightly decreases with increasing particle diameter (Figure 5f).

An important aspect that becomes evident from the above analysis is that utilizing peak intensity, that is, the absorption

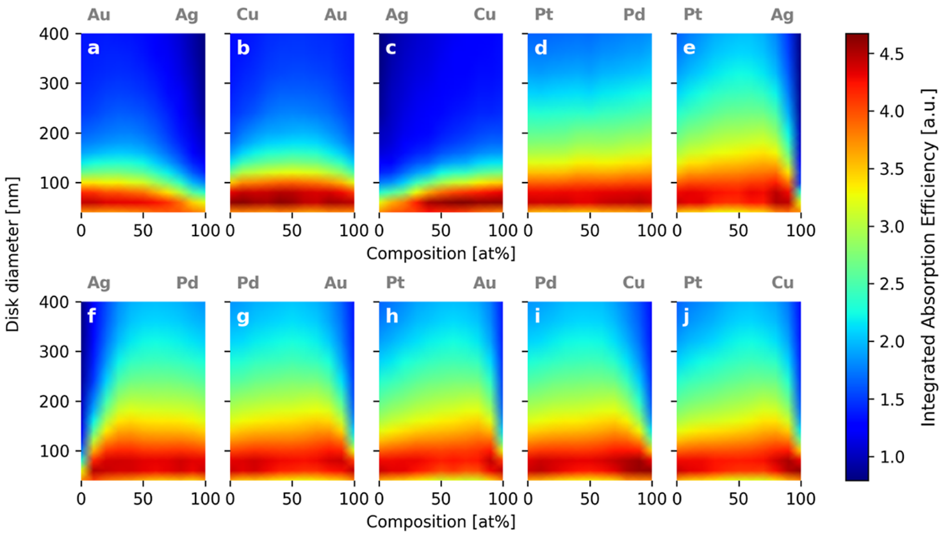

Figure 6. Interpolated integrated absorption efficiency for all 10 considered alloy systems as a function of composition and particle diameter (a−j). As the first key result, most systems exhibit the largest absolute integrated absorption for a disk diameter of ca. 80 nm, except for pure Ag and Ag-heavy isovalent alloys where absorption is maximized for smaller particle sizes. As the second key result, for all systems except PdPt and AgCu, alloys exhibit a higher integrated absorption efficiency than their neat constituents above a particle size of 100 nm. The raw data based on which this figure was composed are summarized in Figure S8 in the Supporting Information.

efficiency value at the spectral position of the LSPR absorption peak maximum, likely is not completely capturing the light absorption properties of these systems—in particular in applications where broad-band illumination is used to, for example, stimulate chemical processes photothermally[11,12] or in photothermal therapy based on light absorbing metal nanoparticles.[13,59] In this context, we therefore argue that spectrally integrated absorption efficiency is a better descriptor of the systems' ability to absorb light. Therefore, we integrated the absorption efficiency from 1.1 to 4.1 eV (ca. 1130 to 300 nm, which corresponds to a slightly extended visible spectral range) for all 10 binary alloy systems calculated and for all particle sizes considered so far. Furthermore, to better resolve possible trends, we added the particle diameters 140, 160, 180, 200, 240, 280, 320, 360, and 400 nm to our analysis (Figure 6). We also note that the obtained spectrally integrated absorption efficiency values are proportional to the absorbed power if one assumes a flat light spectrum. By not including a specific light source and instead showing the integrated absorption efficiency, it is straightforward to project our results on a scenario with a specific light source (spectrum) of interest for a specific application.

The most apparent feature in these data is the red band that signifies the highest integrated absorption and that for the largest fraction of all considered alloy compositions occurs at approximately 80 nm particle diameter, thereby advertising this particle size range as the champion in terms of maximized broad-band absorption for a disk-type particle geometry. Interestingly, a similar optimal size of ca. 70 nm was found for gold nanospheres by Shafiqa et al. and explained by non-radiative absorption being maximized before radiative (scattering) LSPR decay starts to become the dominant channel.[20,60] Hence, we argue that the same reasoning also can be applied here to explain our observations.

Analyzing the different alloys in more detail, for pure Ag and AuAg/AgCu alloys with Ag content of up to 50% (Figure 6a,c), the maximal integrated absorption is shifted to smaller particle diameters and significantly reduced at the absolute level. For neat Ag nanoparticles, this is in agreement with Geonmonond et al. who reported an increased absorption efficiency in the range of 30 nm particle size.[61] As the first reason for this behavior, we identify that Ag, due to its low loss properties in the visible spectral range, only exhibits a significant absorption peak for particles with a diameter <80 nm (cf. Figure 4a) since in larger structures, radiative LSPR decay completely dominates.[20] The second reason is the high energy needed for the excitation of the interband transition from the 4d to the 5sp band in Ag, that is, 3.98 eV, compared to Au where the corresponding 5d to 6sp band transition occurs at significantly lower 2.4 eV[38] and to Cu where the 3d to 4sp transition occurs at 2.15 eV.[37] Focusing on the composition dependence, the key finding for AuAg and AgCu is that absorption is maximized in Au- and Cu-heavy alloys with Ag.

In contrast, AuCu shows an almost constant integrated absorption efficiency across the whole composition range for particles smaller than 80 nm, while for larger sizes, absorption is maximized at ca. 50 at. % (Figure 6b). This is on one hand due to a similar onset of interband transitions in Cu (2.15 eV) and Au (2.4 eV) and on the other hand due to a very similar behavior of the LSPR absorption peak, as discussed above. In general, the isovalent full d-band systems exhibit the largest decline in integrated absorption with increasing particle size.

The isovalent PdPt alloy (Figure 6d) exhibits significant absorption across the entire composition range. However, at the absolute level, it is inferior to the other three isovalent systems AuAg, AuCu, and AgCu for particle sizes <120 nm due to an overall weaker plasmonic excitation. For particle diameters >120 nm, however, the PdPt system outperforms the other three isovalent alloys due to a weaker scattering decay channel that is the consequence of broad-band interband transitions to the unfilled d-bands across the entire considered spectral range. A second key difference compared to the other isovalent systems is the almost constant integrated absorption value across the full composition range and for all sizes, due to the very similar band structure of Pt and Pd (cf. Figure 5c).

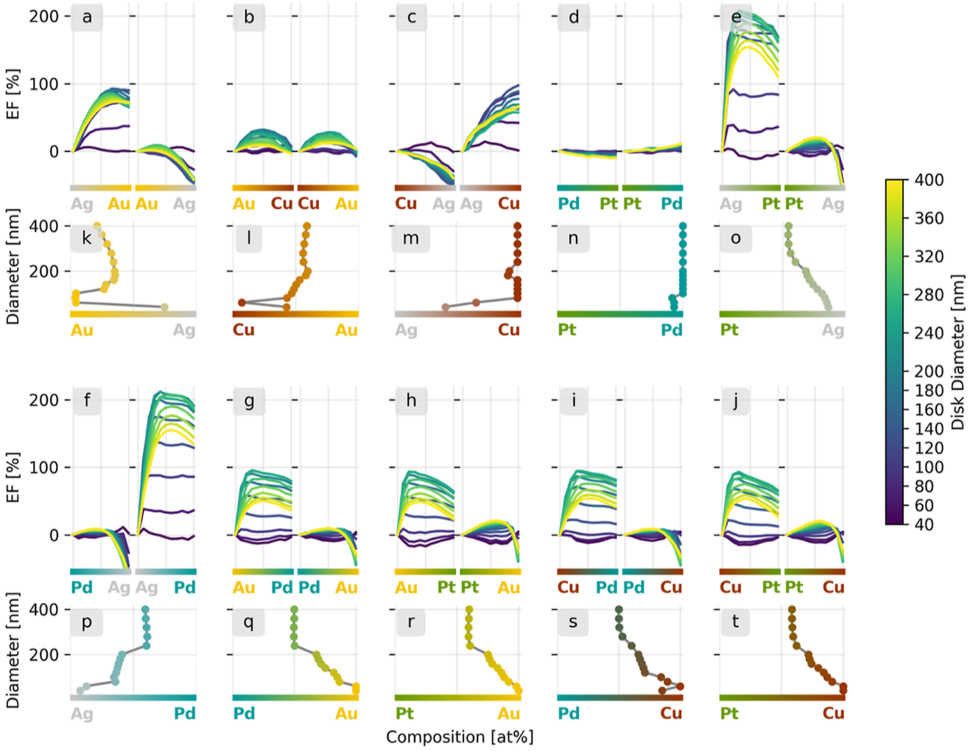

Figure 7. Integrated absorption efficiency enhancement factor, EF, for the entire considered particle size range and for AuAg (a), AuCu (b), AgCu (c), PdPt (d), PtAg (e), AgPd (f), AuPd (g), PtAu (h), PdCu (i), and PtCu (j). The EFs are plotted by taking each of the pure metals of each alloy system as a reference (left and right part of each panel), to explicitly reveal the positive/negative impact of alloying one metal with the other, and vice versa. Alloy composition yielding the highest EF for all considered particle diameters for AuAg (k), AuCu (l), AgCu (m), PdPt (n), PtAg (o), AgPd (p), AuPd (q), PtAu (r), PdCu (s), and PtCu (t). These plots reveal that in most cases, alloying increases the integrated absorption efficiency compared to the neat alloy constituents, and that the alloy composition that features the highest EF shifts with particle diameter. The data are interpolated between 10 at. % steps (for non-interpolated raw data, we refer to Figure S9a−j). Integrated absorption efficiency EF for each alloy system and the entire considered particle size range. The EFs are plotted by taking each of the pure metals of each alloy system as a reference (left and right part of each panel), to explicitly reveal the positive/negative impact of alloying one metal with the other, and vice versa. (k−t) Alloy composition with the highest EF for all considered particle diameters, revealing that in most cases alloying increases integrated absorption efficiency compared to the neat alloy constituents, and that the alloy composition that features the highest EF shifts with particle diameter. The data are interpolated between 10 at. % steps, and for non-interpolated raw data, we refer to Figure S9 in the Supporting Information.

Turning to the non-isovalent systems, we find that they behave similar across the board for all sizes, with a strong increase in integrated absorption between 0 and 30 at. % added Pd or Pt (Figure 6e−j). Hence, when comparing to the isovalent systems AuAg, AuCu, and AgCu, alloying with Pd and Pt increases absorption significantly for particle sizes >100 nm due to the induced absorption peak broadening and the simultaneously reduced radiative LSPR decay.

The most important conclusion from the above detailed analysis of integrated absorption efficiency in our 10 alloy systems is that in most combinations of materials and sizes, it is an alloy that exhibits the highest absolute integrated absorption value and thus outperforms the neat metal constituents. To further analyze and quantify this key finding, we introduce an absorption enhancement factor $\mathrm{EF} = \frac{\int Q_{\mathrm{abs}}}{\int Q_{\mathrm{abs,ref}}} - 100$, where Q_{abs} is the absorption efficiency of the alloy system in question and $Q_{\mathrm{abs,ref}}$ is the absorption efficiency of the chosen pure reference metal. We then calculated EF for a particle diameter range from 40 to 400 nm and for all 10 binary alloys by taking each of the pure metals of each alloy as a reference in two independent calculations, to explicitly reveal the positive/negative impact of alloying one metal with the other and vice versa (Figure 7).

This analysis reveals that Ag, which is a poor absorber below the onset of interband transitions at 3.98 eV, benefits the most from alloying with another metal (Figure 7a,c,e,f). This is particularly pronounced when Ag is alloyed with Pd or Pt due to the induced distinct spectral broadening of the absorption peak and the increased absorption also for large particle sizes due to a suppressed scattering decay channel of the LSPR. The same trends and reasoning can also be applied to Au and Cu, although not as strongly as to Ag (Figure 7b). Consequently, Pt and Pd on the other hand benefit only marginally from being alloyed with Au, Ag, or Cu in terms of integrated absorption efficiency (Figure 7e−j). Interestingly, however, the rule of increased absorption in alloys does not apply for the smallest particle sizes. For the non-isovalent systems (Figure 7e−j), this can be explained by the strong plasmonic absorption peak of Au, Ag, and Cu that "compensates" for the peak broadening induced by alloying. For the isovalent systems on the other hand (Figure 7a−d), the overall similarity of the absorption efficiency spectra is the main reason.

The PdPt system is a further exception from the identified general trends since it for all sizes and compositions essentially lacks any absorption enhancement due to alloying because of the optical similarity of the two systems (Figure 7d). We also note that neat Pd is a marginally better absorber than neat Pt. The AuCu system is another exception but in terms of symmetry of the enhancement with respect to the alloy constituents since it is the only system where both constituents benefit almost equally from being alloyed with the other one (Figure 7b).

As the final step of this analysis, we extracted the composition with the highest EF—and thus also highest integrated absorption—for each alloy type and for all particle sizes (Figure 7). Starting out with the isovalent alloy systems, as the main result for AuAg, this analysis reveals how the alloy composition that maximizes integrated absorption shifts from Ag heavy alloys at small sizes to Au heavy alloy for particles >60 nm, due to the poor absorbing properties of Ag in the large particle size range (Figure 7k). The situation is similar but even more extreme for AgCu, where pure Cu is the best-performing composition for most particle sizes (Figure 7c). AuCu on the other hand shows the best-performing composition close to 50% for almost all sizes (Figure 7b), whereas PdPt shows essentially no benefit of alloying since absorption in pure Pd is only few percent higher than that in Pt (Figure 7d).

Inspecting the non-isovalent systems reveals a clear trend where (i) the full d-band metal (or an alloy composition close to it) experiences the highest EF and where (ii) increasing particle diameter shifts the alloy composition with the highest EF toward 50% (Figure 7o−t). The latter is because for small particle sizes Au, Ag, and Cu and the alloys with high full d-band metal content exhibit significant absorption themselves, which then quite rapidly decreases with increasing particle size at the cost of the scattering LSPR decay channel. Therefore, they benefit both from the broadband interband transitions and absorption peak broadening provided by alloying with Pt or Pd in this particle size regime (cf. Figure 5e). At the absolute level, we also note that for the smallest particle sizes of the non-isovalent alloy absorption enhancement by alloying is only on the order of few percent, whereas it is up to 212% for the champion system AgPd for particle sizes around 180 nm and an Ag content of 40 at. %.

As a general summary of this analysis, we can see that, first, alloying is the most beneficial in terms of maximized absorption efficiency for particle sizes above 60 to 100 nm, depending on the specific system. At these larger sizes, most metal particles experience that scattering becomes the dominant LSPR decay channel, which can be tweaked toward non-radiative absorption by alloying, thereby enhancing the absorption efficiency at these sizes. Second, alloying is most beneficial for the full d-band metals Au, Ag, and Cu, with Ag as the champion, if alloyed with a half full d-band metal-like Pt and Pd. On an absolute scale, the largest increase in the integrated absorption efficiency is obtained for particle sizes at around 180 nm, where Au and Cu show an increase of up to 100% and Ag just over 200%. Notably, even when Ag, Au, and Cu are alloyed with each other, an increased integrated absorption efficiency can be seen, however to a somewhat lesser extent, where AgAu exhibits a maximum increase of almost 100% and AuCu of ca. 30% for particle sizes around 140 nm.

■ CONCLUSIONS

In conclusion, we have presented the systematic screening and a fundamental physics discussion of the light absorption efficiency of 10 binary late transition-metal alloys composed of Au, Ag, Cu, Pd, and Pt, using a combination of FDTD simulations for nanoparticles with 14 different sizes and experimental absorption efficiency measurements on nanofabricated quasi-random alloy nanoparticle array samples with 10 at. % alloy composition intervals. The first key finding is that most alloys exhibit a higher integrated absorption efficiency than their neat constituents, with an enhancement of up to 200% when Ag is alloyed with Pd or Pt for a nanoparticle diameter around 180 nm. This advertises alloying as a means to maximize light absorption in metal nanoparticles. As the second key result, we found that most neat metals and their alloy systems exhibit their highest absolute absorption efficiency for nanoparticles with a diameter of around 80 nm, where the balance between radiative and non-radiative LSPR decay is optimized, except for Ag and Ag-heavy alloys where the optimum is shifted to smaller sizes.

Taken all together, our findings highlight the potential and value of alloying as a handle to engineer the visible light absorption properties of metal nanoparticles. Specifically, for applications where an enhancement of absorption is needed, alloying with Pd and Pt is identified as the most beneficial since adding only few percent to Au, Ag, and Cu increases the absorption efficiency significantly. As an example, we predict such alloying strategies to find applications in plasmonic catalysis as a way to tailor the non-radiative LSPR decay in the quest to distinguish near-field and hot electron-driven reaction pathways.[61]

■ METHODS

Fabrication. The samples were fabricated using hole-mask colloidal lithography on fused silica substrates for spectrophotometry and on oxidized silicon substrates for SEM imaging. For the nanofabrication, the following instrumentation was used: spincoating (Suss, LabSpin6), oxygen ion etching (Plasmatherm, BatchTop m/95), and electron beam evaporation (Lesker, PVD 225). We used a 0.2 wt % 140 nm sulfate latex bead solution (molecular probes by life technologies) in deionized water to create the mask. To induce alloy formation after evaporation, the samples were annealed in a flow reactor for 24 h at 500 °C in 4 ± 0.12% H_2 in Ar carrier gas, at a flow rate of 100 mL/min.

Scanning Electron Microscopy. A Zeiss Supra 55 was used to record the SEM overview images with the in-lens system at an acceleration voltage of 10 kV and at a working distance of at least 5 mm.

Spectrophotometry. Optical absorption spectra of the samples were obtained using a Cary 5000 spectrophotometer with the diffuse reflectance accessory DRA 2500. We used a step width of 1 nm and an averaging time of 0.3 s per step.

Finite-Difference Time-Domain. Ansys-Lumericals FDTD solution version 8.26.2717 was used to calculate the absorption cross section of the alloy nanodisks. The geometry that was simulated was composed of a disk with the diameter ranging from 40 to 400 nm and a height of 25 nm placed on a SiO_2 substrate. For the calculations with the purpose of comparing them to experimental values (cf. Figure 3), the diameters were extracted from SEM images of the experimental samples (see Figure S2). The dielectric functions for the neat metals and alloy systems are obtained from a study by Rahm et al.[33] and for the SiO_2 substrate was taken Ansys-Lumerical's database and originates from a study by Palik[43] As shown in Figure 3c, we used the dielectric function for the metals Au,[41−46] Pd,[42,43,47,48] Pt,[43,48] and Cu.[41−43,46,49] The used source was a total field/scattered field source with a linearly polarized plane wave.

■ ASSOCIATED CONTENT

Supporting Information

The Supporting Information is available free of charge at https://pubs.acs.org/doi/10.1021/acsphotonics.2c01597.

> Comparison of the absorption cross section and the absorption efficiency of Au nanodisks; mean nanoparticle diameter of the three experimentally investigated systems AuPd, AuCu, and PdPt; comparison of scaled and not scaled absorption efficiency spectra obtained by FDTD and experimentally measured; raw data of experimentally measured integrated absorption efficiency; real part of the dielectric functions of 10 alloy systems; LSPR absorption peak positions as a function of particle diameter and alloy composition; density of states of Pd and Pt; raw data of the FDTD-simulated integrated absorption efficiency; and raw data of the best EF as a function of alloy composition for different particle diameters (PDF)

■ AUTHOR INFORMATION

Corresponding Author

Christoph Langhammer − *Department of Physics, Chalmers University of Technology, 412 96 Göteborg, Sweden;* orcid.org/0000-0003-2180-1379; Email: clangham@chalmers.se

Author

Christopher Tiburski − *Department of Physics, Chalmers University of Technology, 412 96 Göteborg, Sweden;* orcid.org/0000-0003-3925-5409

Complete contact information is available at: https://pubs.acs.org/10.1021/acsphotonics.2c01597

Funding

Knut and Alice Wallenberg Foundation project 2016.0210.

Notes

The authors declare no competing financial interest.

■ ACKNOWLEDGMENTS

This research has received funding from the Knut and Alice Wallenberg Foundation project 2016.0210. Part of this work was carried out at the MC2 cleanroom under the umbrella of the Chalmers Excellence Initiative Nano.

■ REFERENCES

(1) Xu, Q.; Liu, F.; Liu, Y.; Cui, K.; Feng, X.; Zhang, W.; Huang, Y. Broadband Light Absorption Enhancement in Dye-Sensitized Solar Cells with Au-Ag Alloy Popcorn Nanoparticles. *Sci. Rep.* **2013**, *3*, 2112.

(2) Pillai, S.; Green, M. A. Plasmonics for Photovoltaic Applications. *Sol. Energy Mater. Sol. Cells* **2010**, *94*, 1481−1486.

(3) Atwater, H. A.; Polman, A. Plasmonics for Improved Photovoltaic Devices. *Nat. Mater.* **2010**, *9*, 205−213.

(4) Hao, J.; Wang, J.; Liu, X.; Padilla, W. J.; Zhou, L.; Qiu, M. High Performance Optical Absorber Based on a Plasmonic Metamaterial. *Appl. Phys. Lett.* **2010**, *96*, 251104.

(5) Xue, T.; Liang, W.; Li, Y.; Sun, Y.; Xiang, Y.; Zhang, Y.; Dai, Z.; Duo, Y.; Wu, L.; Qi, K.; Shivananju, B. N.; Zhang, L.; Cui, X.; Zhang, H.; Bao, Q. Ultrasensitive Detection of MiRNA with an Antimonene-Based Surface Plasmon Resonance Sensor. *Nat. Commun.* **2019**, *10*, 28.

(6) Nugroho, F. A. A. A.; Darmadi, I.; Cusinato, L.; Susarrey-Arce, A.; Schreuders, H.; Bannenberg, L. J.; da Silva Fanta, A. B.; Kadkhodazadeh, S.; Wagner, J. B.; Antosiewicz, T. J.; Hellman, A.; Zhdanov, V. P.; Dam, B.; Langhammer, C. Metal-polymer hybrid nanomaterials for plasmonic ultrafast hydrogen detection. *Nat. Mater.* **2019**, *18*, 489−495.

(7) Liao, H.; Nehl, C. L.; Hafner, J. H. Biomedical Applications of Plasmon Resonant Metal Nanoparticles. *Nanomedicine* **2006**, *1*, 201−208.

(8) Christopher, P.; Xin, H.; Linic, S. Visible-Light-Enhanced Catalytic Oxidation Reactions on Plasmonic Silver Nanostructures. *Nat. Chem.* **2011**, *3*, 467−472.

(9) Linic, S.; Aslam, U.; Boerigter, C.; Morabito, M. Photochemical Transformations on Plasmonic Metal Nanoparticles. *Nat. Mater.* **2015**, *14*, 567−576.

(10) Adleman, J. R.; Boyd, D. A.; Goodwin, D. G.; Psaltis, D. Heterogenous Catalysis Mediated by Plasmon Heating. *Nano Lett.* **2009**, *9*, 4417−4423.

(11) Song, C.; Wang, Z.; Yin, Z.; Xiao, D.; Ma, D. Principles and Applications of Photothermal Catalysis. *Chem. Catal.* **2022**, *2*, 52−83.

(12) Mateo, D.; Cerrillo, J. L.; Durini, S.; Gascon, J. Fundamentals and Applications of Photo-Thermal Catalysis. *Chem. Soc. Rev.* **2021**, *50*, 2173−2210.

(13) Fu, Q.; Zhang, X.; Song, J.; Yang, H.; Key, M. Plasmonic Gold Nanoagents for Cancer Imaging and Therapy. *View* **2021**, *2*, 20200149.

(14) Lee, J.-H.; Choi, J.-W. Application of Plasmonic Gold Nanoparticle for Drug Delivery System. *Curr. Drug Targets* **2018**, *19*, 271−278.

(15) Amendola, V.; Pilot, R.; Frasconi, M.; Maragò, O. M.; Iatì, M. A. Surface Plasmon Resonance in Gold Nanoparticles: A Review. *J. Condens. Matter Phys.* **2017**, *29*, 203002.

(16) Bohren, C. F.; Huffman, D. R.*Absorption and Scattering of Light by Small Particles*; John Wiley & Sons: New York, 1998.

(17) Link, S.; El-Sayed, M. A. Shape and Size Dependence of Radiative, Non-Radiative and Photothermal Properties of Gold Nanocrystals. *Int. Rev. Phys. Chem.* **2000**, *19*, 409−453.

(18) Zorić, I.; Zäch, M.; Kasemo, B.; Langhammer, C. Gold, Platinum, and Aluminum Nanodisk Plasmons: Material Independence, Subradiance, and Damping Mechanisms. *ACS Nano* **2011**, *5*, 2535−2546.

(19) Langhammer, C.; Kasemo, B.; Zorić, I. Absorption and Scattering of Light by Pt, Pd, Ag, and Au Nanodisks: Absolute Cross Sections and Branching Ratios. *J. Chem. Phys.* **2007**, *126*, 194702.

(20) Kolwas, K.; Derkachova, A. Plasmonic Abilities of Gold and Silver Spherical Nanoantennas in Terms of Size Dependent Multipolar Resonance Frequencies and Plasmon Damping Rates. *Opto-Electron. Rev.* **2010**, *18*, 429−437.

(21) Gong, C.; Leite, M. S. Noble Metal Alloys for Plasmonics. *ACS Photonics* **2016**, *3*, 507−513.

(22) Nugroho, F. A. A.; Iandolo, B.; Wagner, J. B.; Langhammer, C. Bottom-Up Nanofabrication of Supported Noble Metal Alloy Nanoparticle Arrays for Plasmonics. *ACS Nano* **2016**, *10*, 2871−2879.

(23) Rebello Sousa Dias, M.; Leite, M. S. Alloying: A Platform for Metallic Materials with On-Demand Optical Response. *Acc. Chem. Res.* **2019**, *52*, 2881−2891.

(24) Ashby, M. F.*Materials: Engineering, Science, Processing and Design*; Butterworth-Heinemann: Cambridge, 2018.

(25) Soares, C.*Gas Turbines*; Elsevier: Oxford, 2015.

(26) Singh, A. K.; Xu, Q. Synergistic Catalysis over Bimetallic Alloy Nanoparticles. *ChemCatChem* **2013**, *5*, 652−676.

(27) Darmadi, I.; Khairunnisa, S. Z.; Tomeček, D.; Langhammer, C. Optimization of the Composition of PdAuCu Ternary Alloy Nanoparticles for Plasmonic Hydrogen Sensing. *ACS Appl. Nano Mater.* **2021**, *4*, 8716−8722.

(28) Wang, H.; Gang, H.; Wei, D.; He, Y.; Issaka Alhassan, S.; Yan, L.; Wu, B.; Cao, Y.; Jin, L.; Huang, L. Bismuth−titanium alloy nanoparticle@porous carbon composite as efficient and stable Cl-storage electrode for electrochemical desalination. *Sep. Purif. Technol.* **2022**, *296*, 121375.

(29) Huynh, K.-H.; Pham, X.-H.; Kim, J.; Lee, S. H.; Chang, H.; Rho, W.-Y.; Jun, B.-H. Synthesis, Properties, and Biological Applications of Metallic Alloy Nanoparticles. *Int. J. Mol. Sci.* **2020**, *21*, 5174.

(30) Lerch, S.; Stolaś, A.; Darmadi, I.; Wen, X.; Strach, M.; Langhammer, C.; Moth-Poulsen, K. Robust Colloidal Synthesis of Palladium-Gold Alloy Nanoparticles for Hydrogen Sensing. *ACS Appl. Mater. Interfaces* **2021**, *13*, 45758−45767.

(31) Thota, S.; Wang, Y.; Zhao, J. Colloidal Au-Cu alloy nanoparticles: synthesis, optical properties and applications. *Mater. Chem. Front.* **2018**, *2*, 1074−1089.

(32) Zhang, L.; Xie, Z.; Gong, J. Shape-controlled synthesis of Au-Pd bimetallic nanocrystals for catalytic applications. *Chem. Soc. Rev.* **2016**, *45*, 3916−3934.

(33) Rahm, J. M.; Tiburski, C.; Rossi, T. P.; Nugroho, F. A. A.; Nilsson, S.; Langhammer, C.; Erhart, P. A Library of Late Transition Metal Alloy Dielectric Functions for Nanophotonic Applications. *Adv. Funct. Mater.* **2020**, *30*, 2002122.

(34) Jian, C. C.; Zhang, J.; Ma, X. Cu-Ag Alloy for Engineering Properties and Applications Based on the LSPR of Metal Nanoparticles. *RSC Adv.* **2020**, *10*, 13277−13285.

(35) Berciaud, S.; Cognet, L.; Tamarat, P.; Lounis, B. Observation of Intrinsic Size Effects in the Optical Response of Individual Gold Nanoparticles. *Nano Lett.* **2005**, *5*, 515−518.

(36) Christensen, N. E. The Band Structure of Silver and Optical Interband Transitions. *Phys. Status Solidi B* **1972**, *54*, 551−563.

(37) Hollstein, T.; Kreibig, U.; Leis, F. Optical Properties of Cu and Ag in the Intermediate Region between Pure Drude and Interband Absorption. *Phys. Status Solidi B* **1977**, *82*, 545−556.

(38) Kolwas, K.; Derkachova, A. Impact of the Interband Transitions in Gold and Silver on the Dynamics of Propagating and Localized Surface Plasmons. *Nanomaterials* **2020**, *10*, 1411.

(39) Fredriksson, H.; Alaverdyan, Y.; Dmitriev, A.; Langhammer, C.; Sutherland, D. S.; Zäch, M.; Kasemo, B. Hole-Mask Colloidal Lithography. *Adv. Mater.* **2007**, *19*, 4297−4302.

(40) Tiburski, C.; Boje, A.; Nilsson, S.; Say, Z.; Fritzsche, J.; Ström, H.; Hellman, A.; Langhammer, C. Light-Off in Plasmon-Mediated Photocatalysis. *ACS Nano* **2021**, *15*, 11535−11542.

(41) Babar, S.; Weaver, J. H. Optical Constants of Cu, Ag, and Au Revisited. *Appl. Opt.* **2015**, *54*, 477.

(42) Johnson, P. B.; Christy, R. W. Optical Constants of the Noble Metals. *Phys. Rev. B* **1972**, *6*, 4370−4379.

(43) Palik, E. D.*Handbook of Optical Constants of Solids*; Academic Press: Orlando, 1998; Vol. *1*−3.

(44) *CRC Handbook of Chemistry and Physics*, 102nd ed.; Rumble, J. R., Ed.; CRC Press/Taylor & Francis: Boca Raton, Florida, 2021.

(45) Hagemann, H. J.; Gudat, W.; Kunz, C. Optical Constants from the Far Infrared to the X-Ray Region: Mg, Al, Cu, Ag, Au, Bi, C, and Al2O3. *J. Opt. Soc. Am.* **1975**, *65*, 742−744.

(46) McPeak, K. M.; Jayanti, S. v.; Kress, S. J. P.; Meyer, S.; Iotti, S.; Rossinelli, A.; Norris, D. J. Plasmonic Films Can Easily Be Better: Rules and Recipes. *ACS Photonics* **2015**, *2*, 326−333.

(47) Palm, K. J.; Murray, J. B.; Narayan, T. C.; Munday, J. N. Dynamic Optical Properties of Metal Hydrides. *ACS Photonics* **2018**, *5*, 4677−4686.

(48) Werner, W. S. M.; Glantschnig, K.; Ambrosch-Draxl, C. Optical Constants and Inelastic Electron-Scattering Data for 17 Elemental Metals. *J. Phys. Chem. Ref. Data* **2009**, *38*, 1013−1092.

(49) Querry, M. R.*Optical Constants. Contractor Report CRDC-CR-85034*, 1985.

(50) Yakubovsky, D. I.; Arsenin, A. v.; Stebunov, Y. v.; Fedyanin, D. Yu.; Volkov, V. S. Optical Constants and Structural Properties of Thin Gold Films. *Opt. Express* **2017**, *25*, 25574.

(51) Olmon, R. L.; Slovick, B.; Johnson, T. W.; Shelton, D.; Oh, S. H.; Boreman, G. D.; Raschke, M. B. Optical Dielectric Function of Gold. *Phys. Rev. B: Condens. Matter Mater. Phys.* **2012**, *86*, 235147.

(52) Peña-Rodríguez, O.; Pal, U. Effects of Surface Oxidation on the Linear Optical Properties of Cu Nanoparticles. *J. Opt. Soc. Am. B* **2011**, *28*, 2735−2739.

(53) Ciesielski, A.; Skowronski, L.; Trzcinski, M.; Górecka, E.; Trautman, P.; Szoplik, T. Evidence of Germanium Segregation in Gold Thin Films. *Surf. Sci.* **2018**, *674*, 73−78.

(54) Mayrhofer, K. J. J.; Hartl, K.; Juhart, V.; Arenz, M. Degradation of Carbon-Supported Pt Bimetallic Nanoparticles by Surface Segregation. *J. Am. Chem. Soc.* **2009**, *131*, 16348−16349.

(55) Lesina, A. C.; Vaccari, A.; Berini, P.; Ramunno, L. On the Convergence and Accuracy of the FDTD Method for Nanoplasmonics. *Opt. Express* **2015**, *23*, 10481.

(56) Maier, S. A.*Plasmonics: Fundamentals and Applications*; Springer: New York, 2007.

(57) Dekura, S.; Kobayashi, H.; Kusada, K.; Kitagawa, H. Hydrogen in Palladium and Storage Properties of Related Nanomaterials: Size, Shape, Alloying, and Metal-Organic Framework Coating Effects. *ChemPhysChem* **2019**, *20*, 1158−1176.

(58) Krupski, K.; Moors, M.; Jóźwik, P.; Kobiela, T.; Krupski, A. Structure Determination of Au on Pt(111) Surface: LEED, STM and DFT Study. *Materials* **2015**, *8*, 2935−2952.

(59) Jaque, D.; Martínez Maestro, L.; del Rosal, B.; Haro-Gonzalez, P.; Benayas, A.; Plaza, J. L.; Martín Rodríguez, E.; García Solé, J. Nanoparticles for Photothermal Therapies. *Nanoscale* **2014**, *6*, 9494−9530.

(60) Shafiqa, A. R.; Abdul Aziz, A.; Mehrdel, B. Nanoparticle Optical Properties: Size Dependence of a Single Gold Spherical Nanoparticle. *J. Phys. Conf.* **2018**, *1083*, 012040.

(61) Geonmonond, R. S.; daSilva, A. G. M.; Rodrigues, T. S.; deFreitas, I. C.; Ando, R. A.; Alves, T. v.; Camargo, P. H. C. Addressing the Effects of Size-Dependent Absorption, Scattering, and Near-Field Enhancements in Plasmonic Catalysis. *ChemCatChem* **2018**, *10*, 3447−3452.

https://doi.org/10.1021/acsphotonics.2c01597